RSC Advances

PAPER

View Article Online
View Journal | View Issue

Cite this: *RSC Adv.*, 2024, **14**, 11932

The engineering of defect-modified boron nitride ribbons: an effective adsorbent to rapid capture for tetracycline

Xi Chen,[ab] Yufei Tang, *[a] Zhangwen Xie,[a] Wanxing Zheng,[a] Xiuying Lin,[a] Yang Tie,[a] Qian Liang,[a] Zhuangzhuang Zhang,[a] Zhaowei Liu[a] and Kang Zhao [a]

Antibiotics, the persistent organic pollutants, have brought serious pollution to the aquatic environment. Therefore, it is necessary to select rapid adsorbents to remove them from their long-term threat. Herein, the introduction of defects in BN was employed to enhance its surface chemical activity for rapid capture of tetracycline *via* hydrothermal and calcination methods. The defect content in BN can be controlled by adjusting the volume ratio of ethanol to water. Among them, when the volume ratio of H_2O/ethanol is 4/1 (BN-3), BN-3 has the most N defects at 33%, which increases the adsorption rate of h-BN for TC and promotes the adsorption capacity to 302.15 mg g^{-1}, which is due to the introduction of nitrogen defects significantly regulates the electronic structure of BN. The corresponding theoretical calculations confirm that BN with N defects decreases the absorption energy of BN for TC. Additionally, the adsorption removal rate of tetracycline still reached 95.5% after 5 cycles of TC adsorption by BN-3, indicating that the defect-modified BN has good reusability and is beneficial for its use in pollutant adsorption.

Received 13th March 2024
Accepted 9th April 2024

DOI: 10.1039/d4ra01941e

rsc.li/rsc-advances

Introduction

Antibiotics, as highly effective antimicrobial agents, growth additives in animal husbandry, and aquaculture agents in the control of human and animal disease, have wide applications.[1] However, as antibiotics enter the organisms, most of them drain the ecosystem in the form of prodrugs or metabolites.[2] Among them, tetracycline (TC) has been applied in large quantities as a typical antibiotic due to its high antimicrobial activity, low cost, and few side effects, which has caused great harm to human health, and ecological balance.

Adsorption is widely used for the removal of antibiotic contaminants due to its significant advantages such as ease of operation, high recoverability, and high removal capacity.[3–6] Commonly used adsorption materials mainly include activated carbon,[7] MOFs,[8] metallic materials,[9] Natural clay minerals,[10] polymers,[11] and covalent organic frameworks (COFs)[12] The adsorption capacity of these materials is mainly related to their structural and physicochemical properties, among them, hexagonal boron nitride (h-BN), as a graphite-like layered structural material, consists of layers of BN hexagonal units that interact with each other through van der Waals forces.[13–17] It can effectively adsorb antibiotics containing aromatic ring structures through mechanisms such as π–π stacking[18] and hydrogen bonding interactions.[19] However, the lack of active sites on the h-BN surface slowed down the reaction rate of the adsorbed substances on its surface, which led to the desorption of the adsorbed substances on its surface, seriously affecting the final adsorption effect. It has been shown that the introduction of defects in BN can increase the chemical activity of its surface and contribute to a rapid increase in the adsorption rate in the early stages of adsorption.[20] For example, Xiong, *et al.*[21] fabricated boron-containing defective BN, and the adsorption capacity of dibenzothiophene (DBT) reached 43.6 mg S g^{-1} within 40 min. In addition, Chao, *et al.*[22] controllably synthesized h-BN with N vacancies by using di-boron trioxide and urea as reactants, and the base potassium hydroxide as a defect guide. Compared to that of pure BN, the adsorption efficiency of TCs by BN with N defects increased by 18%, which was due to the variable electronic structure of BN. However, the influence of defect content on BN adsorption performance in these studies is absent, and there is a significant decrease in adsorption performance after cyclic adsorption.

Therefore, the defective BN was prepared using a two-step method combining hydrothermal and calcination methods using boric acid, polyvinylpyrrolidone (PVP), and melamine as co-reaction sources to rapidly capture TC and improve reusability. The defect content of the BN could be adjusted by changing the volume ratio of ethanol and water. Among them, when the ratio of water/ethanol was 4/1 (BN-3), which had the most nitrogen (N) defects (33%), the adsorption rate of h-BN on TC was effectively increased, which in turn led to an adsorption

[a]*Department of Materials Science and Engineering, Xi'an University of Technology, China*

[b]*School of Material Science and Engineering, Xi'an University of Technology, China*

capacity of 302.15 mg g^{-1}. In addition, theoretical calculations and experimental results confirmed that the introduction of N defects significantly modulated the electronic structure of BN, which improved the efficiency of its charge separation and migration. The adsorption removal of tetracycline using BN-3 was still as high as 95.5% after 5 TC cycles, which indicates that the defect-modified BN has good reusability and facilitates its use in pollutant adsorption.

Experimental section

Materials

Melamine ($C_3N_6H_6$), boric acid (H_3BO_3), and anhydrous ethanol (CH_3CH_2OH) were procured from Tianjin Shengao Chemical Reagent Co., Ltd. Polyvinylpyrrolidone (PVP) and tetracycline (TC) were all obtained from Tianjin Damo Chemical Reagent Factory. All chemicals used were of analytical reagent grade and were utilized without any further purification before use.

Experimental method

Firstly, 0.35 g of boric acid, 0.31 g of melamine and 0.133 g of polyvinylpyrrolidone (PVP) were mixed and dissolved in a mixture of 30 mL of deionized water and ethanol, in which the volume ratios of water and ethanol were (0 : 5, 1 : 4, 4 : 1, 5 : 0), and then the mixed solution was transferred to a polytetrafluoroethylene liner in a hydrothermal reaction at 160 °C for 12 h. The white products were obtained by naturally cooling, vacuum filtration, and drying at 90 °C for 12 h. Finally, the defective boron nitride was successfully prepared by calcination at 1100 °C for 2 h under N_2 atmosphere. The samples obtained with different volume ratios of water and ethanol were labeled by BN-1, BN-2, BN-3, and BN-4, respectively.

Adsorption measurements

5–300 mg L^{-1} of TC solution was fabricated and was kept in the shade. Then, 10 mg adsorbent was added into 50 mL TC solution and stood for 3 days to reach adsorption equilibrium. During the adsorption, more than 1 mL solution then was separated by a 0.22 μm microporous filter and measured by the UV-vis spectrophotometer (TC: $\lambda = 358$ nm). During the cyclic experiment, 40 mg adsorbent was used and dispersed into 200 mL TC solution (40 mg L^{-1}). Then, the mixed solution was stirred at 25 °C for 120 min for absorption. After absorption, the adsorbent was separated by vacuum filtration. Finally, the obtained product was dried for further use.

Characterization

The phase structures and morphologies of the samples were characterized in detail by X-ray diffraction (XRD, Bruker D8) and scanning electron microscopy (SEM; JSM 6700F, Japan), respectively. The chemical state of the surface elements and their functional groups were analyzed in depth by X-ray photoelectron spectroscopy (XPS, EscaLab 250) and Fourier transform infrared spectroscopy (FTIR, Vatar 360). The specific surface areas and pore distributions were evaluated by an automated physicochemical adsorption isothermometer (iQ-1900, Quantachrome, USA). In addition, the residual concentration of the adsorbed contaminants was determined using a UV-visible spectrophotometer (UV-8000S, Hitachi, Japan) to assess the adsorption performance of the samples. To understand the interaction between TC molecule and N defect-modified BN, a series of theoretical models based on Density Functional Theory (DFT) were carried out. Gaussian 16 software was implemented to realize the geometry optimization, static total energy calculations, and electron density difference calculations. Spin-unrestricted DFT calculations were performed using the DMol^3 code, employing the generalized gradient approximation (GGA)-based Perdue–Burke–Ernzerhof (PBE) as the exchange–correlation generalized function. Dual numerical plus polarisation (DNP) was used for isotropic electron calculations.

Results and discussions

Firstly, the physical phase compositions and surface groups of the defective BN with different H_2O/ethanol volume ratios were investigated, in Fig. 1. As can be seen from Fig. 1(a), all the samples showed obvious characteristic diffraction peaks at $2\theta = 25.4°$ and 42.5°, which corresponded to the (002) and (100) crystal planes of h-BN (JCPDS: 34-0412), respectively, and no other impurity peaks were found. The intensity of the characteristic diffraction peaks increases and then decreases with the increase of water content, and the BN-3 has the strongest (002) crystal plane diffraction peak. This is because the water molecules can participate in the formation process of the BN crystal structure when water is used as a solvent, which is beneficial to the growth and alignment of the crystals. However, when only ethanol is involved in the synthesis of BN as a solvent, it will change the solvent environment of the reaction system, which will lead to an uneven rate of crystal growth or an increase in the number of lattice defects, and thus reduce the crystallinity of the BN. Compared with BN obtained from pure water, when ethanol and water are used as a mixed solvent, its crystallinity is relatively high due to the mixed solvent of ethanol and water can regulate the polarity and solubility of the solvent, which is beneficial for controlling the crystal growth rate, lattice arrangement, and crystal morphology, and thus improve the crystallinity. The main peak of BN-3 is shifted to the lowest angle in contrast to the standard PDF card, which may be attributed to the increase in defects caused by the moderate introduction of ethanol.

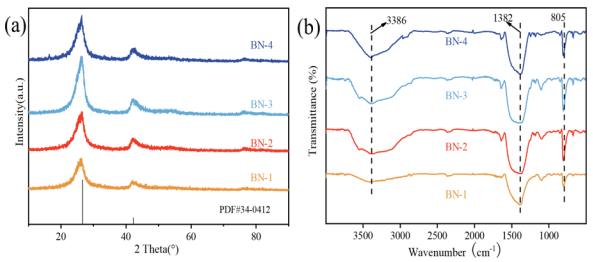

Fig. 1 (a) XRD patterns and (b) FT-IR spectra of BN with different H_2O/ethanol volume ratios.

All the samples were further analyzed for functional groups, as shown in Fig. 1(b). Significant absorption peaks at 3368 cm^{-1}, and 1382 cm^{-1} correspond to the –OH group; and the stretching vibration of the B–N bond. The 805 cm^{-1} belongs to the bending vibration of B–N–B.[23] In addition, the OH groups increase significantly with the increase in the proportion of water, indicating that the synthesis of BN is affected by the polarity and solubility of the mixed solution.

Fig. 2 shows the microscopic morphologies of BN with different water and ethanol volume ratios. From Fig. 2(a), it can be seen that the microscopic morphology of BN-1 consists of many disordered, interlaced, and aggregated nanoribbons. When the volume ratio of H_2O/ethanol is 1 : 4 (BN-2) (Fig. 2(b)), the nanoribbons gradually broaden and self-assemble to form bouquets. When the ratio of H_2O/ethanol is further adjusted to 4 : 1 (BN-3) (Fig. 2(c)), the nanoribbons begin to curl, and the bouquets are still present. However, when the solvent is entirely water (BN-4) (Fig. 2(d)), the nanoribbons are severely agglomerated and become smaller in the radial direction, and the bouquets disappear. It can be seen that the volume ratio of ethanol and water has a greater effect on the morphology of BN nanoribbons. This is due to the formation of supramolecular material ($C_3N_6H_6 \cdot 2H_3BO_3$) through hydrogen bonding of boron nitride precursor molecules in the hydrothermal reaction. In pure ethanol, the relatively small polarity of the solvent cannot effectively dissociate and stabilize the $C_3N_6H_6 \cdot 2H_3BO_3$ supramolecule, and the interactions between the nanoribbons are weak, making it difficult to form an ordered structure. The polarity of the solvent increases with the increase of water content. Water molecules are more polar than ethanol[24] and can more obviously interact with $C_3N_6H_6 \cdot 2H_3BO_3$ molecules. And the formed hydrogen bonds between water molecules and $C_3N_6H_6 \cdot 2H_3BO_3$, further promote the aggregation and orderly arrangement of the nanoribbon structures. The polarity of water is greatest when the solvent is entirely water. The interaction between the water molecules and the boron nitride precursor molecules becomes very strong, leading to severe aggregation of the nanoribbons.

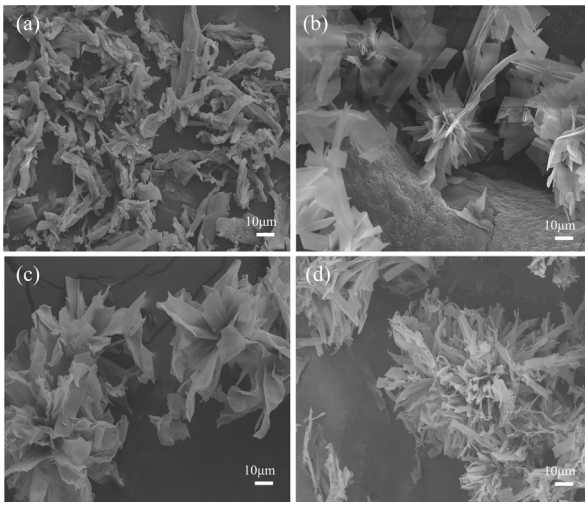

Fig. 2 The morphologies of BN with different H_2O/ethanol volume ratio: (a) BN-1; (b) BN-2; (c) BN-3; and (d) BN-4.

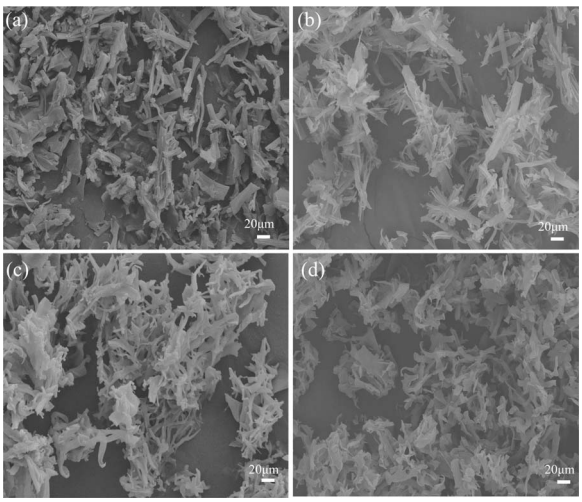

Fig. 3 The morphologies of BN obtained at different H_2O/ethanol volume ratios without PVP (a) BN-1; (b) BN-2; (c) BN-3; and (d) BN-4.

Besides them, the impact of PVP on the morphologies of BN at different H_2O/ethanol volume ratios was also observed, as shown in Fig. 3. Many disordered, interlaced, and aggregated nanoribbons in all samples can be observed due to the absence of dispersivity, which suggests PVP also plays an important to the morphologies of BN nanobelts.

The chemical compositions and surface morphological states of the four samples were further investigated by XPS analysis. As shown in Fig. 4(a), it can be seen that all the prepared samples have the presence of four elements of B, N, C, and O elements, indicating the successful preparation of BN. From the B 1s spectra in Fig. 4(b), it can be seen that the peak at 189.82–190.4 eV corresponds to the B–N bond in BN-1, BN-2, BN-3, and BN-4. Meanwhile, the peaks at 191.47–192.18 eV suggest the presence of B_2O_3. However, the locations of the B–N bond are shifted to the lower binding energy with the increase

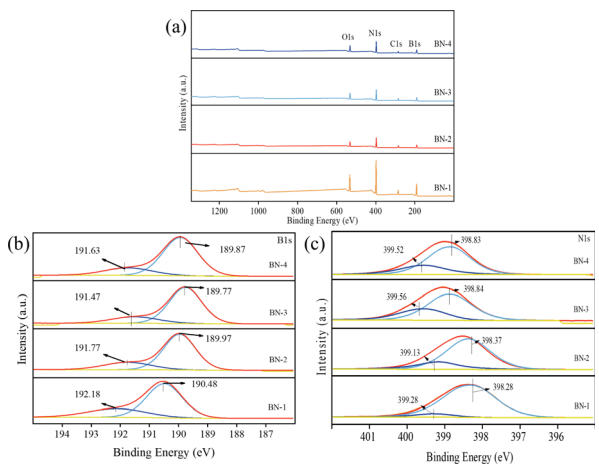

Fig. 4 XPS of BN obtained at different H_2O/ethanol volume ratios (a) full spectrum, (b) B 1s spectrum, and (c) N 1s spectrum.

in water content. Among them, BN-2 has the largest shift, which suggests that the structural defects of the N atoms lead to an increase in the electron density of the B atoms and the largest increase in electron density at BN-3. By splitting the peak area, we estimated the content of N defects,[25] which were 10.4%, 21.6%, 33.2%, and 28.1% for N 1s spectra of BN-1, BN-2, BN-3, and BN-4. Combined with the XRD and SEM results, it can be seen that the lattice arrangement and crystal morphology of BN are affected by the different solvent mixtures of ethanol and water and the presence of PVP. When the proper H_2O/ethanol volume ratio and PVP were added, the lattice arrangement of the BN precursor can be influenced, and there is a carbothermal reduction reaction during calcination due to the presence of PVP, which in turn induces the formation of defects in h-BN.[26] Therefore, the defect content of BN can be regulated by different H_2O/ethanol volume ratios. Among them, BN-3 has the largest N defect content, which is due to the largest degree of lattice defects at an H_2O/ethanol ratio of 4 : 1.

The specific surface area of the material usually plays a significant influence on the adsorption performance. Therefore, N_2 adsorption–desorption isothermal curves were used to study the specific surface area and pore size distribution of all samples, as shown in Fig. 5. It can be seen that the specific surface areas of BN gradually increase with the increase of water content from Fig. 5(a). All samples show typical class IV isothermal curves, with the isotherm starting to increase at $P/P_0 = 0$, and showing an obvious hysteresis in the range of P/P_0 from 0.45 to 1.0, which indicates that there is a mesoporous structure on the surface of the material, and that the BN-4 has the largest specific surface area of 132.52 $m^2\ g^{-1}$, which may lead to the inhibition of the self-assembly process of the nanoribbon structure and fast growth due to a smaller polarity, thus limiting the increase of the specific surface area (Table 1).

Adsorption isotherms are an important means of characterizing the surface properties and affinities of adsorbents.[27] To investigate the absorption relationship between BN and TC, three common isotherm models, Langmuir,[28] Freundlich,[29] and Temkin,[30] were used to fit the experimental data for the calculation in the experiment. From the Langmuir model in Fig. 6(a), the saturated adsorption capacity of BN on TC changed significantly with the addition of the H_2O/ethanol volume ratio. The saturated adsorption capacity of BN-1, BN-2, BN-3, and BN-4 was 229.72 mg g^{-1}, 261.04 mg g^{-1}, 302.15 mg g^{-1}, and 279.52 mg g^{-1}. Among them, BN-3 has the largest saturated adsorption capacity, which is attributed to the increase of the specific area and the N defect content in contrast to those of BN-1 and BN-2. Interestingly, although BN-4 has a higher specific area than that of BN-3, it exhibited a decreased absorption capacity, which is obviously due to the decrease of the N defect content. Therefore, N defect content plays a positive part in the adsorption of TC by decreasing the absorption energy.[31–33] The relevant model parameters are presented in Table 2. All three adsorption isotherm models simulated the adsorption process of the four BN samples adsorbed with TC better. Comparing the adsorption capacities of the four samples at different TC concentrations, the adsorption capacities of the samples increased gradually and non-linearly with the increase of the initial TC concentration. The fitting results in Table 3 show that the fitting coefficients of the three models are above 0.98, and the fitting coefficients of the Langmuir model are slightly higher

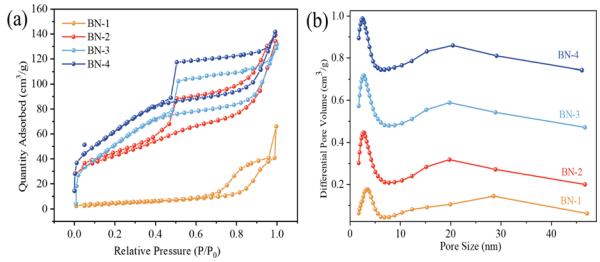

Fig. 5 (a) N_2 adsorption–desorption isotherm and (b) pore diameter distribution of BN with different H_2O/ethanol volume ratios.

Table 1 The specific surface areas, total pore volumes and average pore sizes of BN with different H_2O/ethanol volume ratio

Sample	Specific surface area/$m^2\ g^{-1}$	Total pore volume/$cm^3\ g^{-1}$	Average pore size/nm
BN-1	72.23	0.15	7.79
BN-2	104.22	0.21	5.73
BN-3	127.46	0.22	5.52
BN-4	132.52	0.23	5.57

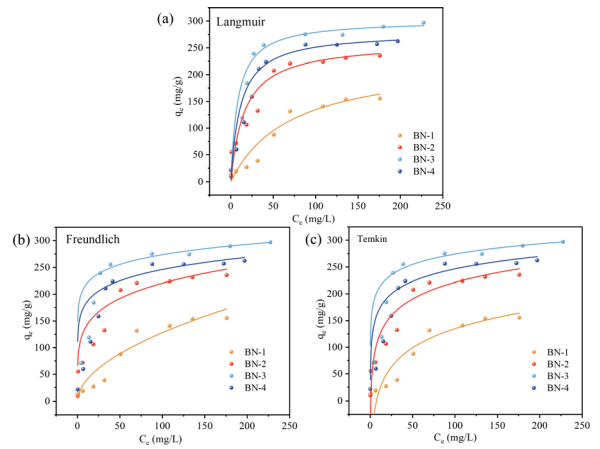

Fig. 6 (a) Langmuir model, (b) Freundlich model, and (c) Temkin model for BN with different H_2O/ethanol volume ratios.

Table 2 Adsorption isotherm model parameters for BN at different H_2O/ethanol ratios

		BN-1	BN-2	BN-3	BN-4
Langmuir	q_m (mg g^{-1})	229.72	261.04	302.15	279.52
	K_L (L mg^{-1})	0.014	0.062	0.12	0.088
	R^2	0.989	0.996	0.998	0.997
Freundlich	K_F	11.09	88.13	173.39	136.36
	$1/n$	0.203	0.412	0.436	0.439
	R^2	0.980	0.989	0.997	0.994
Temkin	K_T (L mg^{-1})	3.81	74.34	145.49	91.52
	R^2	0.987	0.993	0.997	0.995

Table 3 Adsorption kinetics models parameters

		BN-1	BN-2	BN-3	BN-4
	$Q_{e,exp}$ (mg g^{-1})	54.53	108.07	130.73	75.21
Pseudo-first order	$Q_{e,cal}$ (mg g^{-1})	48.71	75.78	108.65	62.29
	K_1 (min^{-1})	0.007	0.012	0.015	0.003
	R^2	0.978	0.985	0.992	0.997
Pseudo-second-order	q_e (mg g^{-1})	48.97	99.81	140.98	74.89
	K_2 (mg g^{-1} min^{-1})	2.91	10.80	14.453	8.915
	R^2	0.981	0.987	0.993	0.998
Intra-particle diffusion	K_{d1} (mg g^{-1} min^{-1})	1.430	3.152	6.513	7.877
	I_1	−0.024	−0.076	−0.048	0.017
	$R_1{}^2$	0.998	0.998	0.9923	0.997
	K_{d2} (mg g^{-1} min^{-1})	1.740	5.127	6.348	5.811
	I_2	7.560	20.057	25.231	35.13
	$R_2{}^2$	0.998	0.982	0.812	0.966
	K_{d3} (mg g^{-1} min^{-1})	1.065	1.526	3.619	1.267
	I_3	16.64	49.604	57.711	58.575
	$R_3{}^2$	0.982	0.781	0.875	0.949

than those of the other two models, which indicates that the Langmuir model can better describe the process of TC adsorption by BN. In the Freundlich model, $1/n$ is less than 1 for all three samples, indicating that the adsorption process is favorable and the adsorption of BN on TC is non-homogeneous surface adsorption. R^2 in the Temkin model is less than 1, which suggests that the TC with adsorbed BN has strong chemisorption properties.

To further investigate the TC adsorption rate and adsorption characteristics of all samples, Fig. 7 showed the fitting results of three kinetic models, and the corresponding parameters are listed in Table 3. In contrast to the pseudo-first-order model, the results of the pseudo-second-order model are closer to the experimental values. This indicates that the adsorption process is dominated by chemisorption. To further investigate the potential rate-controlling steps, an intra-particle diffusion model was carried out in Fig. 7(c). It can be seen that three processes of external mass transfer, intra-particle diffusion, and adsorption of the adsorbate onto the active sites on the inner and outer surfaces of the adsorbent can be divided in the absorption.[18,34] It can be seen that at the beginning of the adsorption, the adsorption capacity rises linearly and the adsorption reaction proceeds faster, with the fastest adsorption rate of BN-4. However, intra-particle diffusion plays a positive part in controlling the rate step. The continued adsorption requires more time for transferring the TC to the interior to bind with the internal sites. At the same time, the TC molecules adhered to the surface of BN, and the adsorption force in the solution produced a repulsive force, so the adsorption rate began to become slow, and BN-4 gradually tended to the equilibrium of the reaction in 60 min. The adsorption rate increases with the increase of ethanol content, the adsorption rate increases with the increase of ethanol content this is because of the high specific surface area and defects provide more adsorption sites. Among them, BN-3 has the fastest adsorption rate. This is because the highest defect content can promote the diffusion and transport of TC molecules inside the material, which makes it easier for the adsorbed molecules to diffuse to the active sites inside the material and improves the adsorption efficiency. Compared to BN-4, BN-with a lower specific area has a greater adsorption capacity and absorption rate than BN-4 due to the higher number of defects, which can increase the effective surface area of BN.

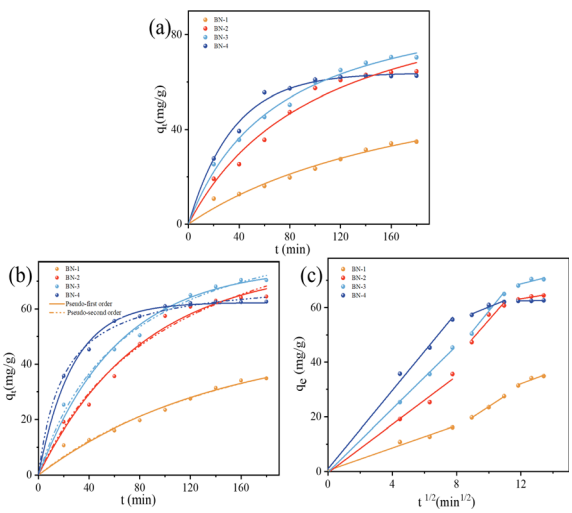

Fig. 7 (a) Adsorption capacity and fitting results of, (b) pseudo-first-order and pseudo-second-order model of, and (c) intra-particle model of TC on BN with various contact times at 20 mg L^{-1} initial concentrations.

To validate the defect-modified BN to enhance the adsorption of TC molecules, a theoretical study on the defect-modified BN was carried out. It was reported that the charge transfer of TC molecules to the BN becomes more pronounced when nitrogen vacancies are present in the BN.[35] Therefore, we mainly simulated the optimized geometries, the electron density difference, and the adsorption energies of the BN with N vacancies, as shown in Fig. 8. The adsorption energy of BN with N vacancies is −1.89 eV, which is lower than that previously reported in the literature,[36] confirming that N vacancies are favorable for BN to adsorb TC molecules. According to Fig. 8(b), it can be seen that the charge transfer of TC molecules to BN becomes more pronounced, suggesting the presence of the dominated chemisorption.

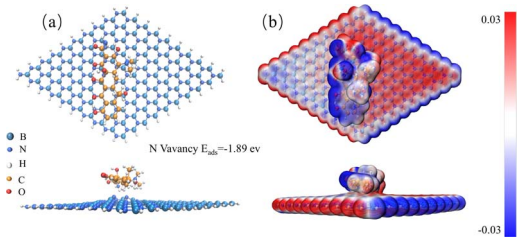

Fig. 8 Theoretical studies adsorption of TC on BN-3 (a) optimized geometries, adsorption energies (b) electrostatic potential (ESP) where blue and red colors indicate regions rich in electrons and deficient in electrons, respectively.

In addition, the adsorption cycle performances of all adsorbents were investigated as shown in Fig. 9. It can be seen that all samples still showed good adsorption performance (more than 90.5%) after three cycles of adsorption. However, the removal rate decreased significantly after the fourth cycle. This decrease may be attributed to the fact that the adsorption sites of BN were gradually saturated after performing four cycles and could not bind more TC molecules. However, BN-3 maintained the removal rate above 95.5% after five cycles with a smaller decrease in the removal rate, indicating that the increase in defect density improved the stability and regeneration of BN.

In natural water systems, various foreign cations and anions commonly coexist, necessitating consideration of the competition between these ions and TC during absorption processes. Given that BN-3 exhibited the highest absorption capacity among the four samples, it was chosen to investigate the impacts of ionic strength and pH on TC adsorption. As shown in Fig. 10, it can be observed that there is no significant competition between cations and TC adsorption, which could be due to that the BN-3 surface with the defects has a positive charge that repels cations, so there are no competing adsorption sites. In contrast, the negatively charged anion will rapidly adsorb to the BN surface, thereby significantly inhibiting the adsorption of TC molecules by BN-3.[37] At the same time, pH also has a large effect on the ability to adsorb TC, as shown in Fig. 10(c). Its adsorption capacity will be significantly reduced in strong acid and alkali environments because H^+ or OH^- ions in solution will competitively adsorb with TC molecules, resulting in the weakening of the interaction between TC molecules and the adsorbent surface, thereby reducing the adsorption performance.

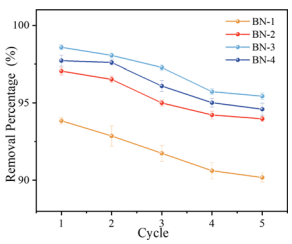

Fig. 9 Reusability of tetracycline (TC) adsorption by BN with different H_2O/ethanol volume ratio.

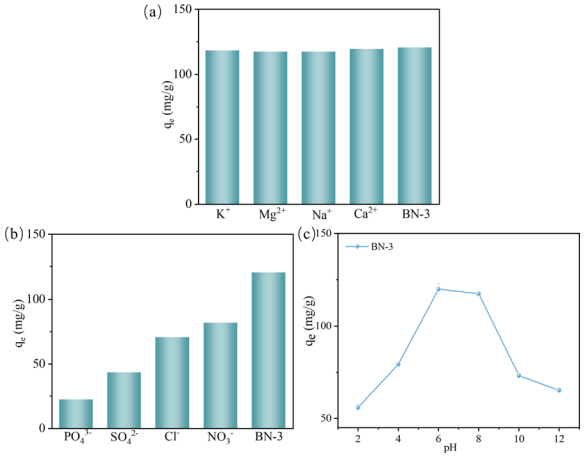

Fig. 10 The effects of (a) 1 mmol cation ions, (b) 1 mmol anion ions, and (c) pH values on the adsorption of TC by BN-3 (T = 25 °C, $C_{(TC)\ initial}$ = 40 mg L^{-1}).

Conclusion

The defective BN was successfully synthesized by a facile hydrothermal and calcination method and the adsorption properties for TC were explored. The N defect was regulated by adjusting the volume ratio of water and ethanol. In particular, the resulting product had the highest N defect content at an H_2O/ethanol ratio of 4 : 1 (BN-3), resulting in a rapid adsorption capacity. Theoretical calculations and experimental results further verified that the introduction of nitrogen defects had a modulating influence on the electronic BN structure, improving its charge separation and migration efficiency. After five TC cycles of adsorption, BN-3 still maintained a high TC adsorption removal rate of 95.5%, which demonstrated that the defect-modified BN had excellent reusability and provided strong support for its application in pollutant adsorption.

Author contributions

Xi Chen: visualization, data curation, formal analysis, writing-original draft preparation. Yufei Tang: conceptualization, methodology, writing-reviewing and editing, funding acquisition. Zhangwen Xie: verification, investigation. Wanxing Zheng: investigation. Xiuying Lin: investigation. Yang Tie: investigation. Qian Liang: investigation. Zhuangzhuang Zhang: investigation. Zhaowei Liu: investigation. Kang Zhao: supervision.

Conflicts of interest

There are no conflicts to declare.

Acknowledgements

This work was supported by National Natural Science Foundation of China (Program No. 52172073) and Scientific Research Program Funded by Education Department of Shaanxi Provincial Government (Program No. 23JC058).

References

1 G. Tan, Y. Mao, H. Wang and N. Xu, *Chem. Eng. Res. Des.*, 2020, **159**, 582–591.
2 J. He, F. Ni, A. Cui, X. Chen, S. Deng, F. Shen, C. Huang, G. Yang, C. Song, J. Zhang, D. Tian, L. Long, Y. Zhu and L. Luo, *Sci. Total Environ.*, 2020, **701**, 134363.
3 Y. Liang, Q. Zhang, S. Li, J. Fei, J. Zhou, S. Shan, Z. Li, H. Li and S. Chen, *J. Hazard. Mater.*, 2022, **423**, 127181.
4 Z. Zhao, B. Liang, M. Wang, Q. Yang, M. Su and S. Liang, *Chem. Eng. J.*, 2022, **427**, 130943.
5 J. Chen, J. He, Z. Yin, T. Wang, S. Liu and S. Cao, *Ceram. Int.*, 2023, **49**, 22139–22148.
6 P. Arabkhani and A. Asfaram, *J. Hazard. Mater.*, 2022, **429**, 128289.
7 W. Ding, G. Zhou, S. Wen, J. Yin, C. Liu, Y. Fu and L. Zhang, *Bioresour. Technol.*, 2022, **360**, 127544.
8 Z.-Y. Zeng, D.-D. Zhou, S.-T. Yang, M.-M. Su and Z.-H. Yang, *J. Environ. Chem. Eng.*, 2023, **11**, 111336.
9 Y. Wang, D. Han, Z. Wang and F. Gu, *ACS Appl. Mater. Interfaces*, 2023, **15**, 22085–22100.
10 L. Wang, J. Cheng, Z. Jin, Q. Sun, R. Zou, Q. Meng, K. Liu, Y. Su and Q. Zhang, *Fuel*, 2023, **344**, 127919.
11 R. S. Bangari and N. Sinha, *J. Mol. Liq.*, 2019, **293**, 111376.
12 Y. Zhao, H. Gu, Y. Zhou, C. Wen, X. Liu, S. Wang, Z. Chen, H. Yang and X. Wang, *J. Environ. Sci.*, 2024, **141**, 63–89.
13 E. Janzen, H. Schutte, J. Plo, A. Rousseau, T. Michel, W. Desrat, P. Valvin, V. Jacques, G. Cassabois, B. Gil and J. H. Edgar, *Adv. Mater.*, 2023, 2306033.
14 C. Martínez-Jiménez, A. Chow, A. D. Smith McWilliams and A. A. Martí, *Nanoscale*, 2023, **15**, 16836–16873.
15 J. S. Algethami, K. K. Yadav, A. Gacem, I. H. Ali, S. Rezania, M. S. O. Alhar, A. Mezni, B.-H. Jeon and S. Chaiprapat, *Environ. Sci. Pollut. Res.*, 2023, DOI: **10.1007/s11356-023-28134-3**.
16 R. Han, J. Ren, Z. Zhou, G.-X. Chen and Q. Li, *ACS Appl. Mater. Interfaces*, 2023, **15**, 34064–34074.
17 M. Shakourian-Fard and G. Kamath, *Phys. Chem. Chem. Phys.*, 2017, **19**, 4383–4395.
18 Q. Song, J. Liang, Y. Fang, Z. Guo, Z. Du, L. Zhang, Z. Liu, Y. Huang, J. Lin and C. Tang, *Chem. Eng. J.*, 2020, **394**, 124985.
19 Z. Liu, K. Zhao, D. Li and Y. Tang, *J. Am. Ceram. Soc.*, 2021, **104**, 1601–1610.
20 Y. Li, L. Liu, H. Yu, Y. Zhao, J. Dai, Y. Zhong, Z. Pan and H. Yu, *Sci. Total Environ.*, 2022, **811**, 151384.
21 J. Xiong, J. Di, W. Zhu and H. Li, *J. Energy Chem.*, 2020, **40**, 99–111.
22 Y. Chao, J. Zhang, H. Li, P. Wu, X. Li, H. Chang, J. He, H. Wu, H. Li and W. Zhu, *Chem. Eng. J.*, 2020, **387**, 124138.
23 Z. F. Wu, L. Guo, K. Cheng, F. Zhang and R. F. Guan, *Ceram. Int.*, 2016, **42**, 4171–4175.
24 J. Zhu, X. Cao and J. Li, *Langmuir*, 2022, **38**, 13910–13915.
25 G. Azuara-Tuexi, E. Muñoz-Sandoval and R. A. Guirado-López, *Phys. Chem. Chem. Phys.*, 2023, **25**, 3718–3736.
26 Z. Tian, K. Chen, S. Sun, J. Zhang, W. Cui, Z. Xie and G. Liu, *J. Adv. Ceram.*, 2019, **8**, 72–78.
27 S. Hosseini, F. Eghbali Babadi, S. Masoudi Soltani, M. K. Aroua, S. Babamohammadi and A. Mousavi Moghadam, *Process Saf. Environ. Prot.*, 2017, **109**, 387–399.
28 X. Dao, H. Hao, J. Bi, S. Sun and X. Huang, *Ind. Eng. Chem. Res.*, 2022, **61**, 6028–6036.
29 L. Zhang, Z. Xin, X. Fei, H. Luo, H. Li, B. Lu, Z. Li and G. Wei, *J. Water Supply: Res. Technol.–AQUA*, 2019, **68**, 39–50.
30 H. Wang, C. Fang, Q. Wang, Y. Chu, Y. Song, Y. Chen and X. Xue, *RSC Adv.*, 2018, **8**, 16260–16268.
31 S. S. Dindorkar, R. V. Patel and A. Yadav, *Colloids Surf., A*, 2022, **643**, 128795.
32 W. Gao, Z. Lin, H. Chen, S. Yan, H. Zhu, H. Zhang, H. Sun, S. Zhang, S. Zhang and Y. Wu, *J. Anal. Appl. Pyrolysis*, 2022, **167**, 105700.
33 C. Chen, Y. Hang, H. S. Wang, Y. Wang, X. Wang, C. Jiang, Y. Feng, C. Liu, E. Janzen, J. H. Edgar, Z. Wei, W. Guo, W. Hu, Z. Zhang, H. Wang and X. Xie, *Adv. Mater.*, 2023, **35**, 2303198.
34 Q. Song, Y. Fang, Z. Liu, L. Li, Y. Wang, J. Liang, Y. Huang, J. Lin, L. Hu, J. Zhang and C. Tang, *Chem. Eng. J.*, 2017, **325**, 71–79.
35 M. Shakourian-Fard, S. Maryamdokht Taimoory, H. R. Ghenaatian, G. Kamath and J. F. Trant, *J. Mol. Liq.*, 2022, **349**, 118122.
36 L. Li, X. Yu, X. Yang, Y. Fang, X. Zhang, X. Xu, P. Jin and C. Tang, *J. Mater. Chem. A*, 2016, **4**, 15631–15637.
37 S. Wang, M. Hao, D. Xiao, T. Zhang, H. Li and Z. Chen, *Chin. J. Chem. Eng.*, 2023, **59**, 200–209.